Ultrafast Inside-Out NMR Assessment of Rechargeable Cells

Roberta Pigliapochi,[a, b] Stefan Benders,[a] Emilia V. Silletta,[a, c, d] Stephen L. Glazier,[e] Elizabeth Lee,[e] Jeff Dahn,[e] and Alexej Jerschow*[a]

Rechargeable battery cells are notoriously difficult to analyze. Conductive casings and the close spacing between electrode layers prevent the penetration of radiofrequency into the active compartment, and thus preclude direct nuclear magnetic resonance studies of cells unless they are specifically designed for such studies. Recently, an inside-out magnetic resonance imaging (MRI) method was developed that allowed measuring the magnetic field distributions in the volume surrounding the cells, and inferring internal parameters, such as the state of charge and current distributions. While the imaging approach provides a potentially very detailed picture of internal mechanisms, it can often be sensitive to background gradients and can be slow. In this work, an alternative approach is presented, which is based on the acquisition of free induction decays in the sample volume surrounding the cells. The signals encode intrinsic battery properties via the induced magnetic fields from the battery materials. A large range of cells were studied with different cathode materials, electrolyte amounts and cycle numbers (age). The spectroscopic signatures from these studies are shown to provide strong classification power for cathode materials. In addition, the derived principal components follow distinct pathways as a function of state of charge. The method is simple and fast (completes in less than a second), and requires only minimal hardware.

1. Introduction

Recent battery failures have highlighted the need for advanced, fast, and nondestructive battery diagnostics.[1–3] *In-situ* NMR spectroscopy and MRI imaging have provided new insights into electrochemical processes, including the examination of lithium microstructure growth and the study of intercalation and conversion processes.[4–8] Radiofrequency penetration problems have often limited the applicability of nuclear magnetic resonance (NMR) spectroscopy in battery diagnostics to the use of devices specifically built for such studies. The recent development of inside-out magnetic resonance imaging (ioMRI), by contrast, has provided the capability of measuring the induced and intrinsic magnetic fields originating from battery cell materials and thus bypassing penetration issues.[9] Therefore, the technique became applicable in this form even to commercial-type cells. The schematic setup of an ioMRI experiment is shown in Figure 1. The spins in the detection medium (typically water) sense the
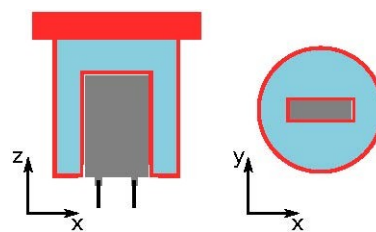
Figure 1. Schematic of the 3D-printed holder setup used for ioMRI (in red). The holder contains the cell (in gray), which is surrounded by the water compartment (in light blue). The holder with the cell inside is placed into an NMR probe with the *z*-axis aligned with the static magnetic field. The vertical cross-section is shown on the left, and the horizontal cross-section is shown on the right.

magnetic field changes surrounding the cell, and these are recorded in MRI-based magnetic field mapping.

This approach enables the assessment of state of charge as well as its distribution across the cell volume.[9,10] The principle of this method is that the battery materials, and notably the cathode component in Li-ion batteries, change their magnetic susceptibility significantly depending on the amount of lithiation.[11–14]

These changes can be detected via small changes in the induced magnetic fields and their distributions even at a distance outside of the cell, as demonstrated by Ilott *et al.*[9] Recently, electrical current distributions were characterized by the measurement of the magnetic field changes surrounding a cell, by employing this same ioMRI approach.[15,16] Strongly magnetic materials, however, which are commonly found in commercial batteries, can distort the images and the derived field maps significantly. These distortions can be corrected using a single-point imaging variant, albeit with some additional overhead in measurement time.[16]

[a] Dr. R. Pigliapochi, Dr. S. Benders, Dr. E. V. Silletta, Prof. A. Jerschow
Department of Chemistry, New York University, 100 Washington Square East, New York, NY, 10003, USA
E-mail: alexej.jerschow@nyu.edu
[b] Dr. R. Pigliapochi
Department of Scientific Research, The Metropolitan Museum of Art, 1000 5th Avenue, New York, NY, 10028, USA
[c] Dr. E. V. Silletta
Universidad Nacional de Córdoba, Facultad de Matemática, Astronomía, Física y Computación, Medina Allende s/n, X5000HUA Cordoba, Argentina
[d] Dr. E. V. Silletta
Instituto de Física Enrique Gaviola, CONICET, Medina Allende s/n, X5000HUA Córdoba, Argentina
[e] Dr. S. L. Glazier, E. Lee, Prof. J. Dahn
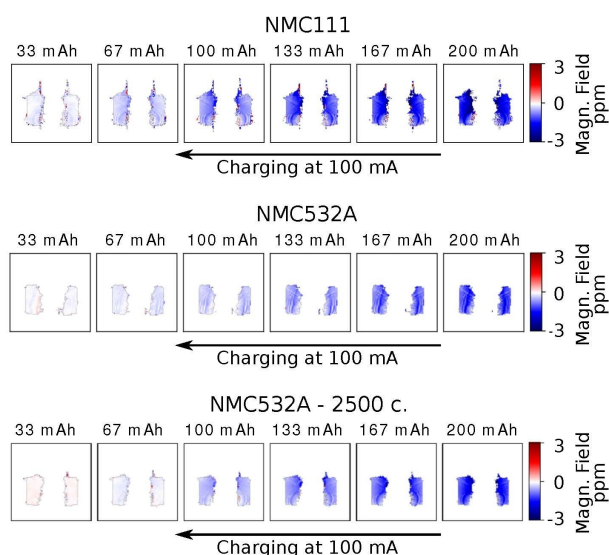Physics and Atmosphere Science, Dalhousie University, Halifax, NS B3H 3J5, Canada

Supporting information for this article is available on the WWW under https://doi.org/10.1002/batt.202000200

Batteries & Supercaps

Articles
doi.org/10.1002/batt.202000200

Chemistry Europe
European Chemical
Societies Publishing

An alternative for cell classification and cell characterization is presented here. By acquiring a free induction decay (FID), instead of acquiring an MRI image, one can observe all the sample-induced effects encoded in one fast single-shot read-out. While site resolution is not possible in this case, we examine here to what extent the information encoded in the FID can be used for cell classification and for the delineation of certain trends. The advantages of this approach are: the method is very fast (completes in less than a second), the technique is even less invasive than ioMRI (no magnetic field gradients needed), can access the fast relaxation regime (and thus is applicable in the presence of larg magnetic field gradients) and it can be performed with very minimal hardware.

We demonstrate here that the technique allows a sensitive classification of samples based on the cathode material in an analysis based on principal components. In addition, the state of charge is clearly reflected in the relative weighting of the principal components along characteristic and distinct pathways for each cathode material.

2. Results and Discussion

FLASH MRI images were collected for every cell during electrochemical charge, as described in the previous section. Three examples are presented in Figure 2, which shows the changes in the field map measured around three cells at discrete steps between 2.5 V and 4.2 V. The maps show a gradual increase of the field during charge, that is directly related to the changes in bulk magnetic susceptibility as an effect of the changes in oxidation states of the electrodes during cycling.[9] Despite the fact that, at each step, the collected field map provides a means to obtain the state of charge and cell condition, Figure 2 also

shows some limitations of the FLASH MRI approach. The magnetic components present in the cell give rise to artifacts in the images, and consequently in the obtained magnetic field maps. These distortions are due to the loss of signal as a consequence of dephasing of the transverse magnetization and additional image misregistration due to strong background gradients.[17] PCA was applied to the MRI results, obtaining a PCA plot with very poor distinction of the different cells and an unclear progression of the points over charge. This finding is believed to be due to the aforementioned limitations of the FLASH MRI sequence itself, mostly due to the long minimal delay (echo time) before signal acquisition can commence. The images appear to lack the ability to capture some distinctive features of the cells, in turn resulting in a poor dataset for cell classification via PCA.

^{1}H NMR spectra were acquired for every cell at different states of charge following the electrochemical cycle between 2.5 V and 4.2 V. Examples are shown in Figure 3.

Overall, all the spectra have a comparable linewidth. The lineshape is generally very broad with some sharper features in the central region, as well as broader features around the center of the peak (Figure 3a), a reflection of the strong
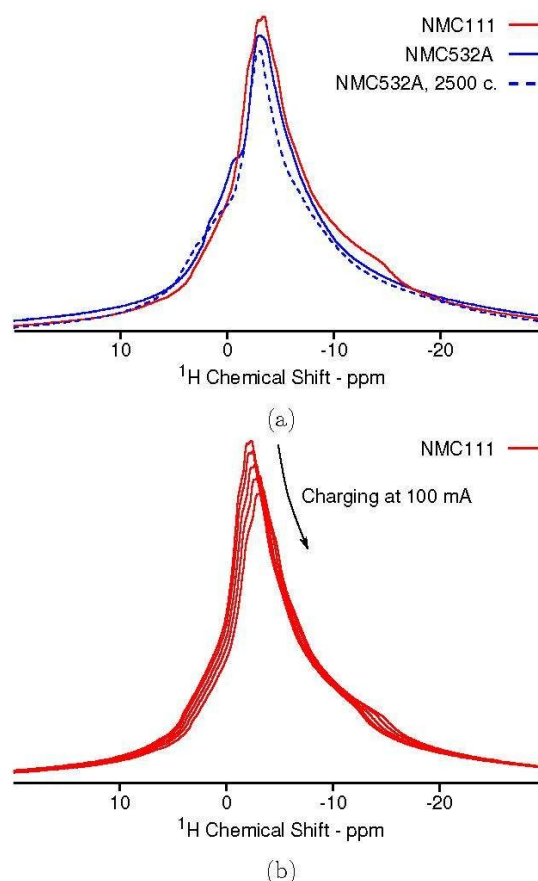

Figure 2. Series of magnetic field maps taken at intervals during the discharge of the following cells: NMC111 (top), NMC532A (middle), and one cell with NMC532A which had undergone 2500 cycles prior to the MRI (bottom).

Figure 3. (a) ^{1}H NMR spectra taken at 2.5 V for cells containing, as cathode: NMC111 (red), NMC532A (solid blue) and NMC532A already undergone 2500 cycles prior to the MRI (dashed blue). (b) ^{1}H NMR spectra taken at intervals during charging of the cell containing NMC111 as cathode. The black arrow shows the direction of shift of the spectra as the cell undergoes charging.

Batteries & Supercaps

Articles
doi.org/10.1002/batt.202000200

Chemistry Europe
European Chemical
Societies Publishing

contributions of the induced and background magnetic fields from the cells. During charging in the electrochemical cycle, one can observe a fairly systematic trend: the ^{1}H NMR spectra for each cell appear to shift overall towards lower ppm values, that is lower resonance frequencies (see Figure 3b). Another common effect found for every cell is a change in lineshape with charging such that the more intense central region of the spectrum gradually decreases in intensity, while the broad and weak feature to either the left or the right of the spectrum increases in intensity. The complexity of the lineshape suggests that each spectrum is the result of the convolution of multiple components, which is expected given the geometry of the arrangement and the dipole fields that would arise from the cell. A deconvolution of peaks was attempted but did not yield any suitable trends due to the fact that many models would fit the data.

The ^{1}H NMR spectra were then studied using principal component analysis (PCA), and the results are shown in Figure 4. A PCA provides a means of classifying a number of measurements based on the few strongest-contributing features of the data set (the principal values). The strength of the approach is that generally a model is not required to perform the classification.

For each cell, the PCA produces a clear trajectory with charging in the score plot, with the sequence of points for every cathode consistent with the change in capacity over cycling. Despite the small overall difference between the spectra (shown in Figure S9), and without any external constraint, the grouping of trends found by the PCA allows for a very distinct classification of cells based on the different cathode materials and charge states (e.g. in the choice of parameter space, the trajectories of cells with the different cathode materials studied here do not cross either.).

A larger set of cells containing the NMC532A cathode was studied, with different amounts of electrolytes and different cycle life in order to test whether the amount of electrolyte or cycle life would have an influence on the classification. Based only on the ^{1}H NMR spectra with no additional constraint, the PCA depicts similar trends for all of the cells containing NMC532A, which are all grouped in a narrow region of the plot. Comparing the PCA results for this group of cells more closely, the trend of the *standard* NMC532A cell (full blue circles in Figure 3) falls in the middle of the series, with the two cells with smaller amounts of electrolyte (open triangles and open diamonds) lying above the *standard* and the cells with a greater cycle life (open squares and stars) lying below the *standard*. Overall, however, all these cells follow similar trajectories in the PCA plot. It is hence concluded that the cathode materials had the strongest influence on the PCA weighting, while the amount of electrolyte and cycle numbers produced comparatively minor variations.

Another interesting feature of the PCA plot is the shape of the curves for each cathode. For both the NMC111 and the whole NMC532A groups, both the principal components 1 and 2 grow with charge. However, the sequence of points for the NMC111 cathode outlines a straighter trend compared to the curved lines for the NMC532A cathode. In contrast to that, principal component 1 grows while component 2 decreases for the cathode materials NMC811 and SC-NMC532 with charge, outlining a sequence of points in the opposite direction to the one of the other two cathodes. This difference does not seem to relate to any obvious differences in the NMR spectra, and the interpretation is made difficult by the fact that the connection between the principal components and the physical properties of the system is yet unknown.

Although methods such as PCA are quite powerful in their ability to classify data, interpreting the scores and the results can be challenging. Similar challenges are faced with other machine learning or neural-network-based algorithms. We have examined the loading plots for the first two principal components (Figure S10), which describe the relative weightings of the respective spectral components that factor into the principal component scores. These plots show that the first principal component generally senses broad spectral features and the global asymmetry of the resonance line (the weighting curve has an odd symmetry), while the second component is sensitive to more localized features and probes predominantly a higher order even symmetry. Changes in charge states would produce overall changes in resonance position and line broadening, and hence, given the symmetry properties probed, it is clear that such effects would be reflected in both principal components, as seen in Figure 4. Likewise, changes in cathode materials change the starting point of each curve.

We further investigated the relationship between FIDs and corresponding PCA plots by progressively removing the first points from the collected FIDs, before processing them. This procedure allows us to determine the maximum allowable pre-acquisition dead-time before the signal acquisition that would still allow a significant level of cell classification in the PCA. This examination was also performed in order to explore why and when an MRI implementation for such classification can fail, since MRI implementations would exhibit significant pre-acquisition delays due to minimally required dead-times (as
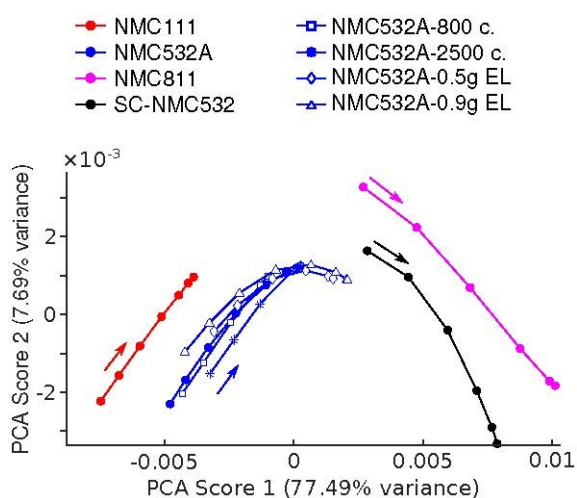
Figure 4. Principal component analysis (PCA) performed on the ^{1}H NMR spectra of all the cells. Each arrow indicates the direction of the trend(s) of the corresponding color as the cell is charged.

Batteries & Supercaps

Articles
doi.org/10.1002/batt.202000200

Chemistry Europe
European Chemical
Societies Publishing

needed for gradient switching and echo delays). The results are shown in the S.I (Figures S2-S8). The PCA results appear largely unchanged upon removal of up to the first 95 μs from the FIDs. This region of the decay is likely to be dominated by the signal originating from the water in high proximity to the most paramagnetic components of the cell, with a resulting fast decay of the NMR signal. This is in agreement with the loss of signal shown in Figure 2 in the proximity of the cells. Up to this pre-acquisition delay, the corresponding NMR spectra appear virtually identical. Beyond this delay and until approximately 305 μs, the PCA plots become progressively harder to interpret, despite some distinction between different cathodes is still present. When the pre-acquisition delay is 455 μs – 955 μs, the PCA plots become non-specific. Interestingly, though, even with such large pre-acquisition delays, successive states of charge of the same cell always result in a clear progression of points in the PCA. Furthermore, since there is a minimum echo time needed to acquire the MRI (2.45 ms fort he experiments shown in Figure 2), it is natural to expect a poor signal contribution coming from zones close to the most paramagnetic components of the cell. This finding indicates that the FID analysis provides information at a time-scale that is inaccessible for the MRI approach. The strong classificaiton power of the FID approach hence derives from the ability to measure the short time-scale behavior. In addition, the speed of the approach, and the minimal hardware requirements are further advantages, which may facilitate wide-spread applications of this approach for the study of fully assembled and enclosed rechargeable cells.

3. Conclusion

In this work, we presented a fast method for cell classification, based on a single-shot free-induction decay NMR spectrum acquisition of the liquid compartments surrounding a cell. These compartments experience a range of magnetic fields due to the presence of the cell and its active material. The changing magnetic susceptibilities due to changes of the oxidation states of the electrode materials (as a function of state of charge) leave their imprints on the spectra. These changes are subsequently analyzed using a principal component analysis algorithm, without additional constraints nor additional *a priori* knowledge. The method is applied on a series of NMC cells, with different cathode materials, electrolyte amounts and cycle life. Cells were prepared with either just a few cycles or a large number of cycles to examine aging or end-of-life scenarios. The resulting PCA trends show the ability to classify the batteries based on their cathode materials, as well as to observe clear trajectories as a function of state of charge. By contrast, the electrolyte amount, or the cell age did not have a strong influence on the classification, with the particular aging model under examination. It is nonetheless possible that other aging processes could be observed with this technique. Overall, the presented method proved to be easy in its implementation, much faster than the respective ioMRI approach, unbiased in the treatment of the data and versatile in its possible extension to *operando* studies.

Materials and Methods

Li-ion Rechargeable Cells

Sealed, dry (no electrolyte), machine-produced 402035-size (240 mAh) pouch cells were purchased from LiFun Technologies (Xinma Industry Zone, Golden Dragon Road, Tianyuan District, Zhuzhou City, Hunan Provence, PRC, 412000). The positive electrodes in these cells used a variety of nickel-manganese-cobalt (NMC) oxides, with different ratios of these transition metals, as follows:

- $LiNi_{0.33}Mn_{0.33}Co_{0.33}O_2$ (NMC111)

- $LiNi_{0.8}Mn_{0.1}Co_{0.1}O_2$ (NMC811)

- Al2O3-coated $LiNi_{0.5}Mn_{0.3}Co_{0.2}O_2$ (NMC532A)

- single-crystal $LiNi_{0.5}Mn_{0.3}Co_{0.2}O_2$ (SC-NMC532)

The positive electrodes were 94% by weight active material with 4% conducting carbon additives and 2% by weight PVDF binder. The negative electrode consisted of 96% artificial or natural graphite (15–30 μm particle size), 2% carbon black, 2% sodium carbon methylcellulose (NaCMC)/styrene butadiene rubber (SBR) binder.[18,19]

Before filling, cells were cut beneath the heat seal and transferred directly into a vacuum oven and heated under vacuum overnight (14 hours) at 100 °C to remove residual moisture. The cells were then transferred into an argon-filled glove box without exposure to air. All cells used in this study underwent the following formation procedure. Cells were filled with 0.5 g, 0.9 g, or 1.0 g of electrolyte as specified throughout. After filling, cells were sealed with a compact vacuum sealer (MSK-115A, MTI Corp.) for 4 seconds at 165 °C, and −90 kPa. Cells were then constrained between two rubber spacers to displace gas formed in the jellyroll during formation. Cells were held at a constant voltage of 1.5 V for 24 hours at room temperature to ensure proper wetting. Cells were then connected to a Maccor 4000 series cycler (Maccor Inc., Tulsa, OK, USA) and charged at their corresponding C/20 rates to 4.2 V, then discharged to 3.8 V at 40 °C. Cells were then transferred to an argon glove box, cut open and re-sealed using the vacuum sealer to release gas produced during formation.

The electrolyte used in cells was prepared with 1.1 m $LiPF_6$ salt (BASF, 99.94%, water content < 14 ppm) in 3:7 weight ratio (3:7) ethylene carbonate (EC): ethyl methyl carbonate (EMC) (BASF, USA, EC purity: 99.95%, EMC purity: 99.99%, water content < 10 ppm) solvent. Electrolyte containing additives was formulated by adding 2% of vinylene carbonate (Novolyte Technologies, Cleveland, OH).[18–20]

Cells that were previously cycled for 800 and 2500 cycles were constrained between rubber shims and connected to a Neware cycler (Neware BTS4000). The NMC532A cell at 800 cycles was cycled between 3.0 V and 4.3 V at a rate of C/3. The NMC532A cell at 2500 cycles was cycled between 3.0 V and 4.1 V at a rate of C/3. The capacity as a function of cycle number for these two cells is shown Figure S1 of the S.I.

Battery Holder

The holder, schematized in Figure 1, was designed using the software Makerbot, following the approach of Ilott *et al.*,[9] and adapted to host the cells used in this study (22 mm length ×7 mm width ×34 mm height). The holder was 3D printed in PLA filament in a hollow cylindrical shape of 39 mm in diameter and 77 mm in length. The void space was filled with a 15 mM aqueous $CuSO_4$ solution. This solution was chosen given the shorter relaxation time ($T_1 = 100$ ms) compared to pure water, which translates to a shorter experimental time. The solution was added in the amount needed

Batteries & Supercaps

Articles
doi.org/10.1002/batt.202000200

Chemistry Europe
European Chemical
Societies Publishing

to fill the void space up to 17 mm height from the bottom of the hollow compartment.

Electrochemistry of the Cells

Every cell was initially fully charged to 4.2 V and subsequently discharged to 2.5 V with a constant current of 100 mA, for a total of three full charge-discharge cycles. Subsequently, each cell was inserted inside the holder and the NMR probe, and was not removed until the end of the experimental procedure. Inside the magnet, each cell was charged in steps of 20 minutes at 100 mA, until the voltage reached 4.2 V. At the end of each 20 minute step, the given cell was allowed to rest for 10 minutes. The 2D MRI and NMR experiments were performed after the resting period, between each 20 minute charging step. A Neware BTS-5V1A potentiostat was used for the electrochemical cycling.

MRI and NMR Experiments

The NMR and MRI experiments were performed on a Bruker Ultrashield 9.4 T Avance I spectrometer operating at 400 MHz for ^{1}H. A Bruker MiniWB57 gradient system (max. gradient strength 0.30 T/m) with a 40 mm ^{1}H birdcage coil was used to acquire both the NMR and the MRI data. After each 20 minute charging and 10 minute rest step, two sets of experiments were performed.

Four consecutive 2D ^{1}H MRI experiments were performed using a slice-selective 2D FLASH sequence implemented in Paravision 5.1, using a hermite pulse shape with pulse duration of 1 ms, an echo time (TE) of 2.45 ms, 2.50 ms, 2.75 ms and 2.80 ms, a repetition time (TR) of 100 ms, a nominal flip angle (α) of 15°, and 12 scans for signal averaging. The field of view (FOV) was 51.2×51.2 mm^2($z \times x$). A **k**-space of 128×128 points resulted in a resolution of 0.4×0.4 mm^2.

After the MRI experiments, a single-pulse NMR experiment was performed using Topspin, with a $\pi/2$ excitation pulse of $\tau_{90} = 30$ µs duration for ^{1}H and one scan.

Before the study of each cell, this series of MRI and NMR acquisitions was performed on the empty holder to obtain the data which would be later used as a reference. Also, shimming is performed at this stage using Paravision 5.1 with the empty holder alone, and was kept unaltered throughout the consecutive study of the given cell. Tuning and matching were adjusted at the end of every charging step.

Processing of the NMR and MRI Data

Imaging data were processed employing an in-house python script. The Fourier transform of each echo **k**-space was subject to noise thresholding and subsequent unwrapping of phase maps. This algorithm, based on the UMPIRE approach,[21] was employed in a way similar to earlier work.[9]

For the single pulse experiments, the data were Fourier transformed and then prepared for the Principal Component Analysis (PCA) by normalizing each magnitude spectrum to its maximum intensity. The PCA algorithm provided by MATLAB[22] was employed to do the statistical analysis with no additional *a priori* information.

Acknowledgements

Conflict of Interest

The authors declare no conflict of interest.

[1] J. W. Gallaway, C. K. Erdonmez, Z. Zhong, M. Croft, L. A. Sviridov, T. Z. Sholklapper, D. E. Turney, S. Banerjee, *J. Mater. Chem. A* **2014**, *2*, 2757–2764.
[2] A. G. Hsieh, S. Bhadra, B. J. Hertzberg, P. J. Gjeltema, A. Goy, J. W. Fleischer, D. A. Steingart, *Energy Environ. Sci.* **2015**, *8*, 1569–1577.
[3] D. S. Eastwood, P. M. Bayley, H. J. Chang, O. O. Taiwo, J. Vila-Comamala, D. J. L. Brett, P. J. Withers, P. R. Shearing, C. P. Grey, P. D. Lee, *Chem. Commun.* **2015**, *51*, 266–268.
[4] R. Bhattacharyya, B. Key, H. Chen, A. S. Best, A. F. Hollenkamp, C. P. Grey, *Nat. Mater.* **2010**, *9*, 504–510.
[5] A. J. Ilott, S. Chandrashekar, A. Klöckner, H. J. Chang, N. M. Trease, C. P. Grey, L. Greengard, A. Jerschow, *J. Magn. Reson.* **2014**, *245*, 143–149.
[6] S. Chandrashekar, N. M. Trease, H. J. Chang, L.-S. Du, C. P. Grey, A. Jerschow, *Nat. Mater.* **2012**, *11*, 311–315.
[7] M. M. Britton, P. M. Bayley, P. C. Howlett, A. J. Davenport, M. Forsyth, *J. Phys. Chem. Lett.* **2013**, *4*, 3019–3023.
[8] O. Pecher, P. M. Bayley, H. Liu, Z. Liu, N. M. Trease, C. P. Grey, *J. Magn. Reson.* **2016**, *265*, 200–209.
[9] A. J. Ilott, M. Mohammadi, C. M. Schauerman, M. J. Ganter, A. Jerschow, *Nat. Commun.* **2018**, *9*, 1–7.
[10] M. Mohammadi, A. Jerschow, *J. Magn. Reson.* **2019**, *308*, 106600.
[11] T. Kadyk, M. Eikerling, *Phys. Chem. Chem. Phys.* **2015**, *17*, 19834–19843.
[12] J. E. Greedan, N. P. Raju, I. J. Davidson, *J. Solid State Chem.* **1997**, *128*, 209–214.
[13] J. T. Hertz, Q. Huang, T. McQueen, T. Klimczuk, J. W. G. Bos, L. Viciu, R. J. Cava, *Phys. Rev. B* **2008**, *77*, 075119.
[14] N. A. Chernova, M. Ma, J. Xiao, M. S. Whittingham, J. Breger, C. P. Grey, *Chem. Mater.* **2007**, *19*, 4682–4693.
[15] M. Mohammadi, E. V. Silletta, A. J. Ilott, A. Jerschow, *J. Magn. Reson.* **2019**, *309*, 106601.
[16] K. Romanenko, P. W. Kuchel, A. Jerschow, *Chem. Mater.* **2020**, *32*, 2107–2113.
[17] K. Romanenko, A. Jerschow, *Proc. Natl. Acad. Sci. USA* **2019**, *116*, 18783–18789.
[18] J. Li, H. Li, W. Stone, S. Glazier, J. R. Dahn, *J. Electrochem. Soc.* **2018**, *165*, A626–A635.
[19] L. M. Thompson, W. Stone, A. Eldesoky, N. K. Smith, C. R. M. McFarlane, J. S. Kim, M. B. Johnson, R. Petibon, J. R. Dahn, *J. Electrochem. Soc.* **2018**, *165*, A2732–A2740.
[20] D. Xiong, J. C. Burns, A. J. Smith, N. Sinha, J. R. Dahn, *J. Electrochem. Soc.* **2011**, *158*, A1431.
[21] S. Robinson, H. Schödl, S. Trattnig, *Magn. Reson. Med.* **2014**, *72*, 80–92.
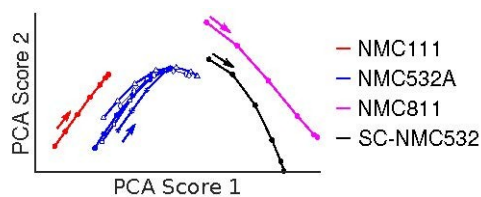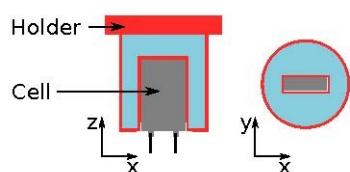[22] *MATLAB Optimization Toolbox*, **2010**.

In a blink: This work presents a technique for ultrafast and nondestructive rechargeable cell diagnostics. The method is based on sensing the changes in the magnetic susceptibility properties of battery materials via nuclear magnetic resonance spectroscopy with minimal hardware. Within less than one second, cells can be classified with regard to cathode material and state of charge. This technique may provide cell diagnostics at different stages of a battery's life cycle.

Dr. R. Pigliapochi, Dr. S. Benders, Dr. E. V. Silletta, Dr. S. L. Glazier, E. Lee, Prof. J. Dahn, Prof. A. Jerschow*

1 – 6

Ultrafast Inside-Out NMR Assessment of Rechargeable Cells